

Guaranteed Set-Membership State Estimation of an Octorotor's Position for Radar Applications

Dory Merhy^a, Cristina Stoica Maniu^a, Teodoro Alamo^b, Eduardo F. Camacho^b, Sofiane Ben Chabane^c, Thomas Chevet^a, Maria Makarov^a and Israel Hinostroza^d

^aUniversité Paris-Saclay, CNRS, CentraleSupélec, Laboratoire des signaux et systèmes, 91190, Gif-sur-Yvette, France; ^bDepartment of Ingeniería de Sistemas y Automática, Universidad de Sevilla, Camino de los Descubrimientos, 41092 Sevilla, Spain; ^cSignal Processing Department, Control Team Parrot Drones, 174-178 Quai de Jemmapes, 75010 Paris, France; ^dUniversité Paris-Saclay, CentraleSupélec, ONERA, SONDRRA, 91190, Gif-sur-Yvette, France

ARTICLE HISTORY

Compiled October 20, 2020

ABSTRACT

In the context of state estimation of dynamical systems subject to bounded perturbations and measurement noises, this paper proposes an application of a guaranteed ellipsoidal-based set-membership state estimation technique to estimate the linear position of an octorotor used for radar applications. The size of the ellipsoidal set containing the real state is minimized at each sample time taking into account the measurements performed by the drone's sensors. Three case studies highlight the efficiency of the estimation technique in finding guaranteed bounds for the octorotor's linear position. The computed guaranteed bounds in the linear trajectory are exploited to find the maximum operating frequency of the radar, a necessary information in radar applications.

KEYWORDS

Set-membership state estimation, linear systems, UAVs, ellipsoidal set, radar application

1. Introduction

State estimation is a major aspect in any process control. Based on available measurements and system knowledge, state estimates can be used for control purposes. Numerous state estimation techniques have been developed throughout the years following two main directions: the stochastic approach and the deterministic approach. The Kalman filter (Kalman, 1960) is a standard method for stochastic state estimation. Nonetheless, the stochastic approach relies on assumptions about noise properties (e.g. Gaussian distribution of perturbations and measurement noises), which could be difficult to verify in practice. Alternatively, the deterministic state estimation approach (Bertsekas & Rhodes, 1971; Fogel & Huang, 1982) using either interval observers (Pourasghar, Puig, & Ocampo-Martinez, 2016) or set-membership¹ estimation

CONTACT Dory Merhy dory.merhy@gmail.com

¹The reader will notice that the notion of set-membership estimation is employed by different research communities (control systems, signal processing, applied mathematics etc.), in a different sense/meaning. In this

techniques (Schweppe, 1968) deals with unknown but bounded disturbances. In set-membership state estimation, various convex² sets are mainly used: *zonotopes* (Alamo, Bravo, & Camacho, 2005; Combastel, 2003; Le, Stoica, Alamo, Camacho, & Dumur, 2013); *polytopes* (Walter & Piet-Lahanier, 1989) and *ellipsoids* (Chernousko, 1994; Daryin & Kurzahnski, 2012; Daryin, Kurzahnski, & Vostrikov, 2006; Durieu, Walter, & Polyak, 2001; Kurzahnski & Vályi, 1996; Polyak, Nazin, Durieu, & Walter, 2004). Due to their simplicity, ellipsoids are widely used in the state estimation literature, while polytopes and zonotopes are used when better accuracy is needed (Puig, 2010; Wang, Puig, Cembrano, & Alamo, 2016). A mixed set-membership state estimation technique combining both zonotopic and ellipsoidal sets is proposed in Ben Chabane, Stoica Maniu, Camacho, Alamo, and Dumur (2016).

In general, it cannot be assumed which approach, either stochastic or deterministic, is better for state estimation. In Merhy, Stoica Maniu, Alamo, Camacho, and Ben Chabane (2017), a comparison in terms of accuracy and complexity between a guaranteed ellipsoidal set-membership state estimation technique and the classic Kalman filter has been made, illustrating the high accuracy that the ellipsoidal method provides. In the same context, a zonotopic Kalman filter has been proposed by Combastel (2015) to benefit from both approaches. In addition, a zonotopic constrained Kalman filter proposed by Merhy, Alamo, Stoica Maniu, and Camacho (2018) where the zonotope is particularly the envelope of the set of constraints applied on the system state at each time instant. Despite the theoretical development of deterministic approaches, there is an obvious gap between theory and practice, and thus the need to apply more accurate recent state estimation techniques on real systems. In this context, the wide use of Unmanned Aerial Vehicles (UAVs) in resource monitoring (Laliberte & Rango, 2009), oil and gas (Hausamann, Zirrig, Schreier, & Strobl, 2005), mapping (Nex & Remondino, 2014) or even for emergencies like forest fire surveillance (Casbeer, Beard, McLain, Li, & Mehra, 2005) attracted more research attention from the scientific community. More specifically, studies related to the need of an accurate knowledge of linear and angular positions of drones are often conducted (Kingston & Beard, 2004). In this context, several approaches have been adopted for the state estimation of a drone. The linear Kalman filter, as well as its extensions to non-linear systems have been widely used in industry to estimate the position of UAVs (De Marina, Pereda, Giron-Sierra, & Espinosa, 2012; Kada, Munawar, Shaikh, Hussaini, & Al-Saggaf, 2016; Teixeira, Tórres, Iscold, & Aguirre, 2011). Alternatively, attempts have been made to bridge the gap between set-membership state estimation theory and practice. For instance, a Zonotopic Extended Kalman Filter (ZEKF) applied to a quadrotor helicopter is presented in Wang and Puig (2016). Moreover, in Garcia, Raffo, Ortega, and Rubio (2015), the results of an interval arithmetics-based estimation technique applied to a quadrotor are compared with the results of a set-membership state estimation technique based on zonotopes. With the proliferation of moderately low cost UAVs, radar-based techniques can be tested on small drones. However, perturbations might cause the deviation of the drones from their planned trajectories leading to an erroneous formation of radar images. Thereby, the use of set-membership state-estimation approaches arises from the need of guaranteed estimates of the system state in the presence of bounded mea-

paper, we focus on set-membership state estimation techniques from the control systems point of view.

²There exist techniques leading to non-convex sets (e.g. based on Taylor models (Paulen, Villanueva, & Chachuat, 2016) or polynomial methods (Streif et al., 2013)) mainly used for parameters estimation, which are beyond the scope of this paper. A brief overview of the set-based parameter estimation methods for nonlinear systems can be found in Chachuat et al. (2015). In addition, stochastic adaptive parameter estimation algorithms were developed (Bhotto & Antoniou, 2011; Lima & Diniz, 2010; Werner, Apolinário Jr, & Diniz, 2007; Werner & Diniz, 2001).

surement noises and perturbations. In order to take advantage of its high accuracy, a guaranteed ellipsoidal set-membership state estimation technique (Ben Chabane, 2015) is applied in this paper on an octorotor. The goal is to guarantee the drone's position when bounded perturbations and measurement noises are considered. Using ellipsoidal representations, the proposed technique computes the set of states that are consistent with the model in a first phase and with the measurements in a second phase such that the system's real state is guaranteed to belong to this set. The advantage of this method lies in the trade-off between its good accuracy and reduced complexity (Ben Chabane, 2015) compared to other techniques in the literature. Indeed, the proposed ellipsoidal state estimation method offers better accuracy than the P -radius based zonotopic state estimation technique (Le et al., 2013) and the three ellipsoidal-based state estimation techniques presented in Ben Chabane, Stoica Maniu, Alamo, Camacho, and Dumur (2014). Using the radar system embedded in the UAV, as well as the estimated coordinates of the drone, an image reconstruction application is exposed to value the efficiency of the set-membership state estimation technique. Furthermore, the relative distance separating the drone from the target is guaranteed to be inside the computed bounds. The relative error done by the estimation leads to the calculation of the operating frequency of the radar. The contribution of this paper is twofold: (i) an extension of a guaranteed ellipsoidal state estimation technique to take possible control signals into consideration; (ii) an application of the method to the position estimation of an octorotor used for radar applications.

As an experimental platform, the Mikrokopter ARF Okto-XL drone (Fig. 1) is used in this paper. The higher payload capacity and the motor redundancy make this octorotor more advantageous over traditional quadrotor aircraft for radar applications. In this context, the UAV is equipped with radar sensors in order to scan large areas and provide high resolution images, thus there is a need for an accurate estimation of the drone's position (i.e. the radar's position) and guaranteed limits for perturbations. The challenge of this estimation problem resides in the model complexity and the possible uncertainties coming from various sources (e.g. measurement noises, perturbations). Previously, a linear Kalman filter and an extended Kalman filter have been designed for the state estimation of the considered octorotor. Then, the proposed filters have been tested on a radar imaging simulator (Chevet, Makarov, Stoica Maniu, Hinostroza, & Tarascon, 2017).

The remainder of the paper is organized as follows. Section 2 briefly recalls the drone's dynamical model. The ellipsoidal set-membership state estimation technique and its advantages are briefly presented in Section 3. The principles of Synthetic Aperture Radar and its applications are shown in Section 4. In Section 5, simulation results are reported illustrating the technique's performance. Finally, in Section 6, conclusion and further developments are proposed.

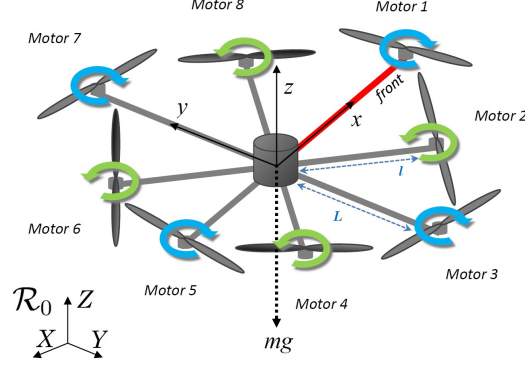


Figure 1. Mikrokopter ARF representation and the associated drone's frame R

Notation. The following symbols a , \mathbf{a} and \mathbf{A} are used to designate a scalar, a vector and a matrix, respectively. The set $\{x \in \mathbb{R} : a \leq x \leq b\}$ defines an *interval*. A *box* $([a_1, b_1], \dots, [a_n, b_n])^\top$ is an interval vector. A unitary interval is denoted by $\mathbf{B} = [-1, 1]$. A box composed of n unitary intervals is a *unitary box* \mathbf{B}^n in \mathbb{R}^n . The identity matrix of size n is denoted by \mathbf{I}_n , while the zero matrix of the same size is denoted by $\mathbf{0}_n$. The symbol \mathbf{A}^\top designates the transpose of the \mathbf{A} matrix. The symbol $\|\mathbf{p}\|$ denotes the Euclidean norm of the vector \mathbf{p} . A symmetric matrix $\mathbf{M} = \mathbf{M}^\top \in \mathbb{R}^{n \times n}$ is called a positive definite matrix, denoted by $\mathbf{M} \succ 0$, if $\mathbf{z}^\top \mathbf{M} \mathbf{z} > 0$, for all vector $\mathbf{z} \in \mathbb{R}^n \setminus \{0_n\}$. A *strip* is defined by the following set $\mathcal{S}(y, \mathbf{d}, \sigma) = \{\mathbf{x} \in \mathbb{R}^n : |y - \mathbf{d}^\top \mathbf{x}| \leq \sigma\}$, where $y \in \mathbb{R}$, $\mathbf{d} \in \mathbb{R}^n$ and $\sigma \in \mathbb{R}_+^*$.

2. Octorotor modeling

The Mikrokopter ARF Okto-XL (Fig. 1) is equipped with an inertial measurement unit (IMU), an altimeter, a GPS and a magnetometer. The drone's microcontroller provides fused and filtered data on its position coordinates (both linear and angular). The measurement data are transferred to the PC through the microcontroller's serial port for off-line data processing.

The octorotor's motion in a state-space representation can be obtained using twelve states: the drone's position in the Earth's frame x , y and z (see Fig. 1), the drone's orientation in the Earth's frame ϕ , θ and ψ , its speed in the same frame V_x , V_y and V_z , and its rotational speed in its own frame ω_x , ω_y and ω_z . This leads to the following state vector $\mathbf{x} = [x \ y \ z \ \phi \ \theta \ \psi \ V_x \ V_y \ V_z \ \omega_x \ \omega_y \ \omega_z]^\top$. The nonlinear dynamical model of the drone used to simulate its behavior is presented in Makarov et al. (2015). However, while this nonlinear model can be useful to evaluate the drone performances in simulation, a simplified linear model Makarov et al. (2015), (Bergman and Ekström (2014), Hoffmann and Waslander (2007)) will be used for the development of linear control laws based on estimation techniques. The model is linearized around the static hovering equilibrium with null translational and rotational velocities and null roll, pitch and yaw angles. The linear general state-space equation can be denoted by

$$\dot{\mathbf{x}}(t) = \mathbf{A}_s \mathbf{x}(t) + \mathbf{B}_s \mathbf{u}(t), \quad (1)$$

with the state vector $\mathbf{x} \in \mathbb{R}^{12}$, the control vector $\mathbf{u} =$

$[F_x^R \ F_y^R \ F_z^R \ \tau_x^R \ \tau_y^R \ \tau_z^R]^\top \in \mathbb{R}^6$, where F_x^R , F_y^R and F_z^R are the components of the resulting propeller's force and τ_x^R , τ_y^R and τ_z^R are the components of the resulting propeller's torque expressed in the drone's frame denoted by the superscript R . The matrices $\mathbf{A}_s \in \mathbb{R}^{12 \times 12}$ and $\mathbf{B}_s \in \mathbb{R}^{12 \times 6}$ are provided in Makarov et al. (2015). The thrust force and drag torque generated by the i -th propeller are assumed to be proportional to the squared propeller's speed Ω_i , with $i = \{1, 2, \dots, 8\}$. The new reduced control vector in this case can be expressed as linear combination of the rotational speeds of the motor Ω_i denoted by the matrix \mathbf{M}_u , leading to $\mathbf{u}(t) = \mathbf{M}_u \mathbf{\Omega}$, with $\mathbf{\Omega} = [\Omega_1 \ \Omega_2 \ \dots \ \Omega_8]^\top$. In order to avoid high computation complexity of the ellipsoidal state estimation method, the 12-state linearized model is decoupled into three double integrator subsystems detailed below.

Continuous-time subsystem 1 (altitude and yaw dynamics dynamics) – It describes the altitude dynamics expressed by the altitude z and the velocity V_z of the drone on this axis as well as the movement of the drone around the vertical axis that changes the direction the drone is pointing to

$$\begin{cases} \dot{z}(t) &= V_z(t), \\ \dot{\psi}(t) &= \omega_z(t), \\ \dot{V}_z(t) &= \frac{1}{m} F_z^R(t), \\ \dot{\omega}_z(t) &= \frac{1}{I_{zz}} \tau_z^R(t). \end{cases} \quad (2)$$

with m the octorotor's mass and I_{zz} the UAV's inertia component around the z-axis.

Continuous-time subsystem 2 (roll and pitch dynamics) – It describes the movement of the drone around the roll axis (front-to-back) and the pitch (side-to-side) axis

$$\begin{cases} \dot{\phi}(t) &= \omega_x(t), \\ \dot{\theta}(t) &= \omega_y(t), \\ \dot{\omega}_x(t) &= \frac{1}{I_{xx}} \tau_x^R(t), \\ \dot{\omega}_y(t) &= \frac{1}{I_{yy}} \tau_y^R(t), \end{cases} \quad (3)$$

with I_{xx} and I_{yy} the UAV's inertia components around the x-axis and the y-axis, respectively.

Continuous-time subsystem 3 (longitudinal dynamics) – It refers to the motion of the drone across the longitudinal axis denoted by the linear coordinates (x

and y) with the corresponding velocities on the two axes (V_x and V_y , respectively)

$$\begin{cases} \dot{x}(t) &= V_x(t), \\ \dot{y}(t) &= V_y(t), \\ \dot{V}_x(t) &= \frac{1}{m} F_x^R(t), \\ \dot{V}_y(t) &= \frac{1}{m} F_y^R(t). \end{cases} \quad (4)$$

However, simplifying conditions should be met for the obtained decoupled model to hold. Indeed, the rotational angles (i.e. roll, pitch and yaw) should be as small as possible and maintained as close as possible to zero. To quantify this constraint, the change in these angles should not exceed 0.2618rad or 15° (Abdolkhosseini, Zhang, & Rabbath, 2013).

The subsystems 1 and 2 describe the angular behavior of the drone, in addition to its altitude, while the subsystem 3 describes the linear movement on both of the x-axis and the y-axis. These subsystems are then discretized with a sampling period T_e which is equal to the highest of all sensors sampling periods. This leads to the state-space representations (5), (6) and (7).

Discretized subsystem 1

$$\begin{cases} \begin{bmatrix} z_{k+1} \\ \psi_{k+1} \\ V_{z_{k+1}} \\ \omega_{z_{k+1}} \end{bmatrix} = \mathbf{A} \begin{bmatrix} z_k \\ \psi_k \\ V_{z_k} \\ \omega_{z_k} \end{bmatrix} + \begin{bmatrix} 0 & 0 \\ 0 & 0 \\ \frac{T_e}{m} & 0 \\ 0 & \frac{T_e}{I_{zz}} \end{bmatrix} \begin{bmatrix} F_z^R \\ \tau_{z_k}^R \end{bmatrix} + \mathbf{E}_1 \mathbf{w}_k, \\ \begin{bmatrix} z_k \\ \psi_k \end{bmatrix} = \mathbf{C} \begin{bmatrix} z_k \\ \psi_k \\ V_{z_k} \\ \omega_{z_k} \end{bmatrix} + \mathbf{F}_1 \mathbf{w}_k. \end{cases} \quad (5)$$

Discretized subsystem 2

$$\begin{cases} \begin{bmatrix} \phi_{k+1} \\ \theta_{k+1} \\ \omega_{x_{k+1}} \\ \omega_{y_{k+1}} \end{bmatrix} = \mathbf{A} \begin{bmatrix} \phi_k \\ \theta_k \\ \omega_{x_k} \\ \omega_{y_k} \end{bmatrix} + \begin{bmatrix} 0 & 0 \\ 0 & 0 \\ \frac{T_e}{I_{xx}} & 0 \\ 0 & \frac{T_e}{I_{yy}} \end{bmatrix} \begin{bmatrix} \tau_{x_k}^R \\ \tau_{y_k}^R \end{bmatrix} + \mathbf{E}_2 \mathbf{w}_k, \\ \begin{bmatrix} \phi_k \\ \theta_k \end{bmatrix} = \mathbf{C} \begin{bmatrix} \phi_k \\ \theta_k \\ \omega_{x_k} \\ \omega_{y_k} \end{bmatrix} + \mathbf{F}_2 \mathbf{w}_k. \end{cases} \quad (6)$$

Discretized subsystem 3

$$\begin{cases} \begin{bmatrix} x_{k+1} \\ y_{k+1} \\ V_{x_{k+1}} \\ V_{y_{k+1}} \end{bmatrix} = \mathbf{A} \begin{bmatrix} x_k \\ y_k \\ V_{x_k} \\ V_{y_k} \end{bmatrix} + \begin{bmatrix} 0 & 0 \\ 0 & 0 \\ \frac{T_e}{m} & 0 \\ 0 & \frac{T_e}{m} \end{bmatrix} \begin{bmatrix} F_{x_k}^R \\ F_{y_k}^R \end{bmatrix} + \mathbf{E}_3 \mathbf{w}_k, \\ \begin{bmatrix} x_k \\ y_k \end{bmatrix} = \mathbf{C} \begin{bmatrix} x_k \\ y_k \\ V_{x_k} \\ V_{y_k} \end{bmatrix} + \mathbf{F}_3 \mathbf{w}_k. \end{cases} \quad (7)$$

The same matrices $\mathbf{A} = \begin{bmatrix} \mathbf{I}_2 & T_e \mathbf{I}_2 \\ \mathbf{0}_2 & \mathbf{I}_2 \end{bmatrix}$ and $\mathbf{C} = [\mathbf{I}_2 \quad \mathbf{0}_2]$ are obtained for the three subsystems. The perturbations and the measurement noises are considered to be modeled by the vector \mathbf{w}_k which is bounded by the unitary box \mathbf{B}^6 and the matrices $\mathbf{E}_i = \epsilon_i \cdot [\mathbf{I}_4 \quad \mathbf{0}_{4 \times 2}]$, $\mathbf{F}_i = \gamma_i \cdot [\mathbf{0}_4 \quad \mathbf{I}_{4 \times 2}]$, for $i \in \{1, 2, 3\}$. The scalars ϵ_i and γ_i represent the accuracy precision provided by the sensors information.

In the following, this octotorotor is the application platform for a guaranteed ellipsoidal set-membership state estimation technique presented in the next section.

3. Guaranteed ellipsoidal set-membership state estimation method

This section briefly describes the ellipsoidal guaranteed state estimation technique (Ben Chabane, 2015) based on the minimization of the radius of the ellipsoidal estimation at each sample time k by solving an optimization problem. Consider the following discrete-time Linear Time Invariant (LTI) system

$$\begin{cases} \tilde{\mathbf{x}}_{k+1} = \mathbf{A} \tilde{\mathbf{x}}_k + \mathbf{B} \tilde{\mathbf{u}}_k + \mathbf{E} \mathbf{w}_k, \\ \tilde{\mathbf{y}}_k = \mathbf{C} \tilde{\mathbf{x}}_k + \mathbf{F} \mathbf{w}_k, \end{cases} \quad (8)$$

where $\tilde{\mathbf{x}}_k \in \mathbb{R}^{n_x}$ is the state vector of the system, $\tilde{\mathbf{u}}_k \in \mathbb{R}^{n_u}$ is the input vector, $\tilde{\mathbf{y}}_k \in \mathbb{R}^{n_y}$ is the measured output vector, and the vector $\mathbf{w}_k \in \mathbf{B}^{n_x+n_y}$ contains the unknown but bounded state perturbations and measurement noises, at sample time k . The matrices \mathbf{A} , \mathbf{B} , \mathbf{C} , \mathbf{E} and \mathbf{F} have the appropriate dimensions. The reader will notice that the discretized subsystems (5), (6) and (7) of the octotorotor are written in the form (8).

Considering that at time instant k the state $\tilde{\mathbf{x}}_k$ belongs to an ellipsoidal set, the main goal is to provide a guaranteed ellipsoidal set-membership estimation for the state $\tilde{\mathbf{x}}_{k+1}$, taking into consideration bounded perturbations and measurement noises (Ben Chabane, 2015). For the ellipsoidal method to be implemented, the initial state is assumed to belong to the ellipsoid

$$\mathcal{E}(\mathbf{P}_0, \bar{\mathbf{x}}_0, \rho_0) = \{\tilde{\mathbf{x}}_0 \in \mathbb{R}^{n_x} : (\tilde{\mathbf{x}}_0 - \bar{\mathbf{x}}_0)^\top \mathbf{P}_0 (\tilde{\mathbf{x}}_0 - \bar{\mathbf{x}}_0) \leq \rho_0\}, \quad (9)$$

with $\mathbf{P}_0 = \mathbf{P}_0^\top \succ 0$ being the shape matrix, $\bar{\mathbf{x}}_0$ the center and the so-called radius ρ_0 (Ben Chabane, Stoica Maniu, Alamo, Camacho, & Dumur, 2014). Similar to the Kalman filter, the algorithm works in a two-step process

- First, the prediction step in which a set offering a bound for the uncertain trajectory of the system is calculated (the blue ellipsoid $\bar{\mathcal{X}}_{k+1}$ in Fig. 2);
- Then, the correction step in which the guaranteed state estimation set at time $k+1$ (the red set $\hat{\mathcal{X}}_{k+1}$ in Fig. 2) is computed as an outer approximation of the intersection (the grey set in Fig. 2) between the predicted state set $\bar{\mathcal{X}}_{k+1}$ and the measurement strip \mathcal{X}_{y_k} (in green in Fig. 2).

Assuming the prior knowledge of $\tilde{\mathbf{x}}_k$ belonging to the ellipsoidal set $\hat{\mathcal{X}}_k$, the predicted state set is given by $\bar{\mathcal{X}}_{k+1} \subseteq \mathbf{A}\hat{\mathcal{X}}_k \cup \mathbf{B}\tilde{\mathbf{u}}_k \cup \mathbf{E}\mathbf{B}^{n_x+n_y}$. This set offers a bound for the uncertain trajectory of the system (8) such that $\tilde{\mathbf{x}}_{k+1} \in \bar{\mathcal{X}}_{k+1}$. This step is followed by the computation of the intersection set between the prediction $\bar{\mathcal{X}}_{k+1}$ and the state calculated with respect to the measurements \mathcal{X}_{y_k} which can be represented by the green strip (Fig. 2). Exhaustively, the grey part (see Fig. 2) is given by $\bar{\mathcal{X}}_{k+1} \cap \mathcal{X}_{y_k}$. Nevertheless, the exact state estimation set that contains $\tilde{\mathbf{x}}_{k+1}$ has in general an arbitrary shape, thus the need of outer-approximating it by an ellipsoid for simplicity reasons ($\hat{\mathcal{X}}_{k+1}$ in Fig. 2). The algorithm is repeated at each iteration step in order to decrease the size of the guaranteed ellipsoidal state estimation set depicted in red in Fig. 2.

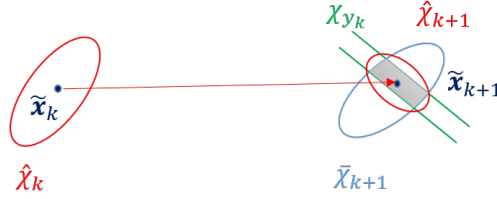


Figure 2. Illustration of the ellipsoidal state-estimation method

Notice that this technique can also be applied on linear time varying systems with interval uncertainties (Ben Chabane, 2015). Even though it is considered to be an important advantage of this method, this characteristic will not be tested in this work. Additionally, the theorems formulating the full solution to this problem are detailed in (Ben Chabane, 2015).

The detailed study considered in Theorem 5.4 of (Ben Chabane, 2015) does not include the input $\tilde{\mathbf{u}}_k$ of the system, which is similar to $\mathbf{B} = \mathbf{0}$. Hence, the present paper deals with the general case when control inputs are considered. Indeed, the system state $\tilde{\mathbf{x}}_{k+1}$ is guaranteed to belong to the ellipsoid $\mathcal{E}(\mathbf{P}_{k+1}, \tilde{\mathbf{x}}_{k+1}, \rho_{k+1})$, with $\mathbf{P}_{k+1} = \mathbf{P}_{k+1}^\top \succ 0$, if: (i) at time k the state $\tilde{\mathbf{x}}_k$ belongs to the ellipsoid $\mathcal{E}(\mathbf{P}_k, \tilde{\mathbf{x}}_k, \rho_k)$ and (ii) there exist a matrix $\mathbf{Y}_{k+1} \in \mathbb{R}^{n_x \times n_y}$, a matrix $\mathbf{G}_{k+1} \in \mathbb{R}^{n_x \times n_x}$, a vector $\mathbf{g}_{k+1} \in \mathbb{R}^{n_x}$ and the strictly positive scalars $\beta_{k+1} > 0$, $\rho_{k+1} > 0$ such that the following Linear Matrix Inequality (LMI) is satisfied

$$\begin{aligned} & \min_{\beta_{k+1}, \mathbf{Y}_{k+1}, \mathbf{P}_{k+1}, \mathbf{G}_{k+1}, \mathbf{g}_{k+1}, \rho_{k+1}} \rho_{k+1} \\ & \text{subject to} \end{aligned} \quad \left\{ \begin{aligned} & \begin{bmatrix} \beta_{k+1} \mathbf{P}_k & 0 & \mathbf{A}^\top \mathbf{P}_{k+1} - \mathbf{C}^\top \mathbf{Y}_{k+1}^\top \\ 0 & \rho_{k+1} - \beta_{k+1} \rho_k & \boldsymbol{\tau}_{k+1}^\top \\ \mathbf{P}_{k+1} \mathbf{A} - \mathbf{Y}_{k+1} \mathbf{C} & \boldsymbol{\tau}_{k+1} & \mathbf{P}_{k+1} \end{bmatrix} \succ 0, \\ & \rho_{k+1} \leq \beta \rho_k + \sigma, \\ & 0 < \beta < 1, \end{aligned} \right. \quad (10)$$

for all \mathbf{w}_k belonging to the vertices set³ of the box $\mathbf{B}^{n_x+n_y}$, with the matrix $\mathbf{Y}_k = \mathbf{P}_k \mathbf{L}_k$, the vector $\boldsymbol{\tau}_{k+1} = (\mathbf{P}_{k+1} \mathbf{A} - \mathbf{Y}_{k+1} \mathbf{C} - \mathbf{G}_{k+1}) \bar{\mathbf{x}}_k + (\mathbf{P}_{k+1} \mathbf{E} - \mathbf{Y}_{k+1} \mathbf{F}) \mathbf{w}_{k+1} - \mathbf{g}_{k+1} + \mathbf{B}(\tilde{\mathbf{u}}_k - \bar{\mathbf{u}}_k)$ and the nominal estimated state $\bar{\mathbf{x}}_{k+1} = \mathbf{P}_{k+1}^{-1} (\mathbf{G}_{k+1} \bar{\mathbf{x}}_k + \mathbf{Y}_{k+1} \tilde{\mathbf{y}}_k + \mathbf{g}_{k+1}) + \mathbf{B} \bar{\mathbf{u}}_k$, where $\bar{\mathbf{u}}_k$ is the nominal control signal.

The proof of this result is similar to the proof provided by (Ben Chabane (2015), page 111) with the additional terms $\mathbf{B} \bar{\mathbf{u}}_k$ in $\boldsymbol{\tau}_{k+1}$ and $\bar{\mathbf{x}}_{k+1}$. Indeed, denoting by $\tilde{\mathbf{z}}_k = \tilde{\mathbf{x}}_k - \bar{\mathbf{x}}_k$ the error between the real state and the nominal estimated state at time k , the goal is to prove the following expression, based on the results proposed in Ben Chabane (2015)

$$\tilde{\mathbf{z}}_k^\top \mathbf{P}_k \tilde{\mathbf{z}}_k \leq \rho_k \Rightarrow \tilde{\mathbf{z}}_{k+1}^\top \mathbf{P}_{k+1} \tilde{\mathbf{z}}_{k+1} \leq \rho_{k+1}.$$

At the time instant $k+1$, the following expression is found

$$\tilde{\mathbf{z}}_{k+1} = (\mathbf{A} - \mathbf{L}_{k+1} \mathbf{C}) \tilde{\mathbf{z}}_k + (\mathbf{A} - \mathbf{L}_{k+1} \mathbf{C}) \bar{\mathbf{x}}_k + (\mathbf{E} - \mathbf{L}_{k+1} \mathbf{F}) \boldsymbol{\omega}_k - \mathbf{P}_{k+1}^{-1} (\mathbf{G}_{k+1} \bar{\mathbf{x}}_k + \mathbf{g}_{k+1}),$$

highlighting that the evolution of the error $\tilde{\mathbf{z}}_{k+1}$ is related to the eigenvalues of the matrix $\mathbf{A} - \mathbf{L}_{k+1} \mathbf{C}$. In addition, the computation of the matrix \mathbf{G}_{k+1} and the vector \mathbf{g}_{k+1} guarantees a faster convergence of the error $\tilde{\mathbf{z}}_{k+1}$ to zero. In this context, the observer (which is similar to the structure of the Luenberger observer) is stable since $\tilde{\mathbf{z}}_k$ converges to zero at each time instant.

Besides minimizing the size of the estimation set by solving the LMI problem (10), this method also reduces the conservativeness of the estimation by allowing the adjustment of the ellipsoid shape. Indeed, considering the matrix \mathbf{P}_{k+1} as a decision variable can modify the shape of the ellipsoid at time instant $k+1$ compared to the ellipsoid at the previous time instant.

Furthermore, the estimation accuracy can be improved by considering additional quadratic constraints on the output measurements $\tilde{\mathbf{y}}_{k+1} = \mathbf{C} \tilde{\mathbf{x}}_{k+1} + \mathbf{F} \mathbf{w}_{k+1}$ and on the perturbations at time instant $k+1$ such that $\mathbf{w}_{k+1}^\top \mathbf{T}_i \mathbf{w}_{k+1} \leq 1$, with $i = 1, \dots, n_x + n_y$, $\mathbf{T}_i = e_i e_i^\top$ and $\mathbf{I}_{n_x+n_y} = [e_1 \dots e_{n_x+n_y}]$. The updated method, improves the accuracy of the estimation by decreasing the size of the ellipsoid $\hat{\mathcal{X}}_{k+1}$ at each iteration. In this context, considering the ellipsoidal state estimation set $\mathcal{E}(\mathbf{P}_{k+1}, \bar{\mathbf{x}}_{k+1}, \rho_{k+1})$ obtained by solving the previous LMI (10), an updated set $\mathcal{E}'(\mathbf{P}'_{k+1}, \bar{\mathbf{x}}'_{k+1}, \rho'_{k+1})$ can be found if the following Linear Matrix Inequality (similar to Ben Chabane (2015), page 118) is satisfied

$$\begin{aligned} & \min_{\rho'_{k+1}, \mathbf{P}'_{k+1}, \mathbf{b}_{k+1}, \mathbf{H}, \theta, \mu_i, \alpha, \gamma} \alpha \\ & \text{subject to} \end{aligned}$$

³Decoupling the 12-state octorotor model into 3 subsystems (5)-(7) allows us to reduce the number of LMI constraints in (10) from $2^{3(n_x+n_y)}$ to $3 \cdot 2^{n_x+n_y}$.

$$\left\{ \begin{array}{l} \left[\begin{array}{ccc} \boldsymbol{\eta}_1 & \boldsymbol{\eta}_2^\top & \mathbf{P}'_{k+1} \\ \boldsymbol{\eta}_2 & \eta_3 - \sum_{i=1}^{n_x+n_y} \mu_i & -\mathbf{b}_{k+1}^\top \\ \mathbf{P}'_{k+1} & -\mathbf{b}_{k+1} & \mathbf{P}'_{k+1} \end{array} \right] \succ 0, \\ \mathbf{P}'_{k+1} \succ 0, \\ \mathbf{F}^\top \mathbf{H} \mathbf{F} < \sum_{i=1}^{n_x+n_y} \mu_i \mathbf{T}_i, \\ \theta \geq 0, \\ \theta < 1, \\ \rho'_{k+1} > \theta \rho_{k+1}, \\ \mu_i \geq 0, \quad i = 1, \dots, n_x + n_y, \\ \gamma > 0, \end{array} \right. \quad (11)$$

with

$$\begin{aligned} \mathbf{b}_{k+1} &= \mathbf{P}'_{k+1} \bar{\mathbf{x}}'_{k+1}, \\ \boldsymbol{\eta}_1 &= \theta \mathbf{P}_{k+1} + \mathbf{C}^\top \mathbf{H} \mathbf{C}, \\ \boldsymbol{\eta}_2 &= -\theta \bar{\mathbf{x}}_{k+1}^\top \mathbf{P}_{k+1} - \tilde{\mathbf{y}}_{k+1}^\top \mathbf{H} \mathbf{C} + \bar{\mathbf{u}}_k^\top \mathbf{B}^\top \mathbf{C}^\top \mathbf{H} \mathbf{C}, \\ \eta_3 &= \rho'_{k+1} - \theta \rho_{k+1} + \theta \|\bar{\mathbf{x}}_{k+1}\|_{\mathbf{P}_{k+1}}^2 + \|\tilde{\mathbf{y}}_{k+1}\|_{\mathbf{H}}^2 + \|\mathbf{C} \mathbf{B} \bar{\mathbf{u}}_k\|^2 - 2 \bar{\mathbf{u}}_k^\top \mathbf{B}^\top \mathbf{C}^\top \mathbf{H} \tilde{\mathbf{y}}_{k+1}. \end{aligned}$$

The proof of this result is similar to Ben Chabane (2015), with the additional terms related to the control signal in $\boldsymbol{\eta}_2$ and η_3 .

Exhaustively, supposing that $\bar{\mathbf{x}}_{k+1} \in \mathcal{E}(\mathbf{P}_{k+1}, \bar{\mathbf{x}}_{k+1}, \rho_{k+1})$, the expression (11) offers an improved ellipsoidal state estimation set $\mathcal{E}'(\mathbf{P}'_{k+1}, \bar{\mathbf{x}}'_{k+1}, \rho'_{k+1})$. Due to the fact that this estimation method changes both the shape and the radius at each iteration k , the computational complexity can be high even though it offers a very good accuracy estimation wise.

The LMI optimization problems (10)-(11) are solved using the `mincx` solver of the Matlab Robust Control Toolbox. This solver is based on the iterative interior point method (Nesterov & Nemirovski, 1994) technique, solving at each iteration a least square problem. Thus, the computational complexity of the ellipsoidal state estimation method can be approximated to $\mathcal{O}(o^{2.75} l^{1.5})$, with o the number of decision variables and l the number of constraints (Vandenberghe & Boyd, 1994) in the worst case scenario. For the optimization problem (10), it should be noted that $o = n_x(1.5n_x + n_y + 1.5) + 4$ and $l = 2^{n_x+n_y} + 3$, while for the improved method represented by the optimization problem (11), $o = n_x(0.5n_x + 2.5) + n_y(0.5n_y + 1.5) + 4$ and $l = n_x + n_y + 6$ which highlights the fact that the improved method offers better accuracy but with higher complexity. This accuracy is further exploited in a radar application which is detailed in the next section.

4. Application to the design of SAR sensor

Synthetic Aperture Radar (SAR) has been proposed in the fifties to provide images of large areas with high resolution (Carrara, Goodman, & Majewski, 1995). Since then, airplanes and satellites have been the main carriers of SAR sensors (Moreira et al., 2013). In recent years, due to reduction in their cost and weight, SAR sensors

are being mounted and tested on small UAVs (Gonzalez-Partida, Almorox-Gonzalez, Burgos-Garcia, & Dorta-Naranjo, 2008; Yan, Guo, Wang, & Liu, 2008; Zaugg, Hudson, & Long, 2006). Moreover, SAR images are formed using the phase evolution resulted from comparing (e.g. via match filtering) a SAR transmitted pulse signal (i.e. typically thousands of pulses per second, hence the term pulse repetition frequency – PRF) with the received scattered signal of the illuminated scatterers of the scene under study (Carrara et al., 1995; Moreira et al., 2013). This is done while the SAR sensor is moving. A popular operating mode for SAR is stripmap (side-looking), where ideally the SAR antenna points to a fixed direction (as illustrated in Fig. 3) and the sensor is assumed to move in a perfect linear trajectory with a constant speed and orientation, which is not the case for the small UAV used in this work. Indeed, even under the best circumstances, perturbations will cause the drone’s path to deviate from its assumed coordinates. As a result, errors might occur in the formation of SAR images if the deviation (e.g. the difference between the ideal and the real UAV’s position) is not accurately taken into account. Errors on the estimation of the position of the SAR sensor (hence, UAV) lead to errors on the relative distance D_r between the SAR sensor and the scatterer (see Fig. 3), which involve a phase error ϕ_e in the SAR data as shown in the next equation

$$\phi_e = \frac{4\pi\delta_D f_0}{c_0}, \quad (12)$$

where δ_D is the error on the estimation of the relative distance $D_r \in [D_{min}, D_{max}]$, f_0 is the working frequency and c_0 is the light speed in free-space (equation adapted from Carrara et al. (1995), page 225) where the working wavelength has been replaced by

$$\lambda = \frac{f_0}{c_0}. \quad (13)$$

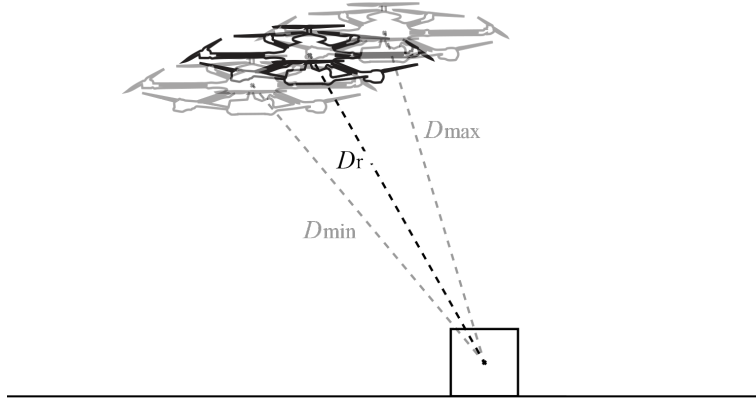


Figure 3. Representation of the drone and the scatterer

In this work, the drone’s linear position is estimated using the ellipsoidal state estimation technique detailed in Section 3. This method offers guaranteed estimation

bounds for the coordinates at each iteration. Thus, the relative distance D_r between the drone and the scatterer can be calculated and bounded by a maximal D_{max} and minimal D_{min} bounds. For instance, the estimation error of the drone's position on both axes induces a relative distance error between the UAV and the scatterer.

The next two figures present examples of SAR images with an accurately estimated UAV position (Fig. 4) and with an erroneous estimated UAV position (Fig. 5). The SAR parameters for these examples are detailed in Table 1. As the Fig. 5 shows, due to phase errors, the position of a single scatterer at 50m range and 2m azimuth with respect to the scanned region can be mistaken as being three scatterers.

Table 1. SAR parameters

PRF	2kHz
Bandwidth	200MHz
Operating frequency	5GHz
Scatterer position	
Azimuth	2m
Ground range	50m

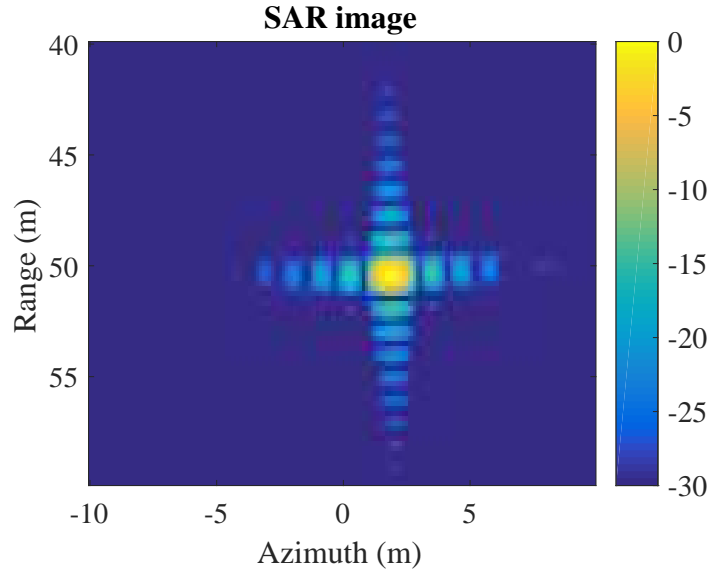


Figure 4. SAR image obtained in the ideal case allowing to correctly identify the scatterer position

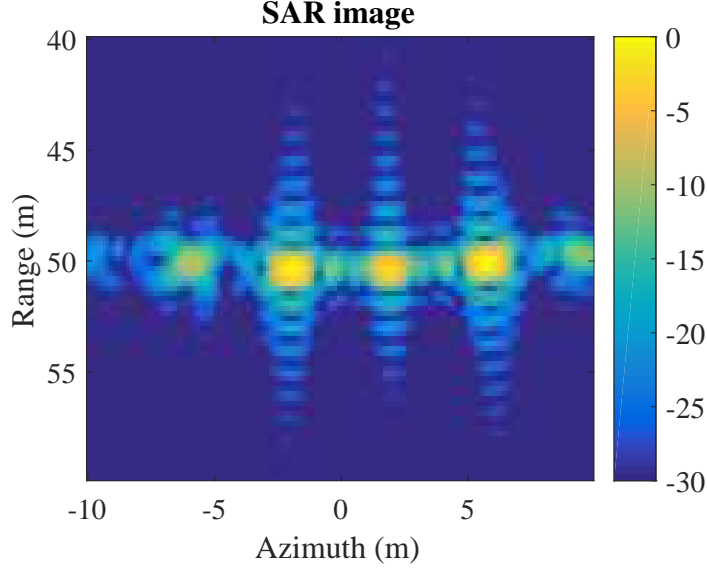


Figure 5. SAR image obtained with an erroneous estimated position

It is common to use signal processing autofocus techniques to compensate these phase errors as long as they are inferior to about 60rad (Carrara et al., 1995). Therefore, according to (12), knowing the maximum error amplitude in the position estimation of the UAV will let us know the maximum working frequency of the SAR sensor. Reciprocally, if the working frequency of the SAR sensor is imposed, this will specify the maximum acceptable error (in terms of guaranteed bounds) of the position estimation of the UAV to obtain SAR images with acceptable performance. In the next section, we will use the guaranteed ellipsoidal state estimation technique to estimate the position of the UAV where the SAR sensors are mounted. This step is followed by the computation of the maximum allowed error amplitude in estimation, in the goal of obtaining the suitable frequencies for which the SAR sensor can operate.

5. Simulation results

The three discretized subsystems (5)-(7) presented in Section 2 are fully controllable and observable. Considering the presence of state perturbations and measurement noises, the complete numerical discrete-time model of the octorotor can be obtained with the drone parameters shown in Table 2 including payload. The sampling period $T_e = 0.1\text{s}$ is the highest of all sensors sampling period. An accuracy of $\pm 1\text{m}$ is assumed for both the GPS and the altimeter, and an accuracy of $\pm 0.01\text{rad}$ is considered for the gyroscope. Based on this information on the bounds of measurement noises and perturbations, the matrices $\mathbf{F}_1 = \mathbf{F}_3 = [\mathbf{0}_4 \quad \mathbf{I}_{4 \times 2}]$ and $\mathbf{F}_2 = 0.01 \cdot [\mathbf{0}_4 \quad \mathbf{I}_{4 \times 2}]$ are chosen. For simplification, the state perturbations can be chosen as follows $\mathbf{E}_1 = \mathbf{E}_2 = \mathbf{E}_3 = 10^{-3} \cdot [\mathbf{I}_4 \quad \mathbf{0}_{4 \times 2}]$. The drone's behavior was simulated using a Matlab/Simulink simulator implementing the non-linear model. Additionally, a linear quadratic integral (LQI) controller, detailed in Makarov et al. (2015) for this UAV is used for nominal input computations. These nominal control inputs are then fed into the linear designed system (5)-(7).

Table 2. Drone parameters

Total mass m	3.69kg
Inertia components	
I_{xx}	0.0869kg·m ²
I_{yy}	0.0873kg·m ²
I_{zz}	0.1683kg·m ²

Two reference trajectories have been tested in the simulation

- A circular trajectory in which the drone rotates around its z-axis at a constant tangential speed;
- A linear trajectory back and forth on the x-axis at a linear constant speed which allows the drone to scan the selected area and process the estimated positions for the radar application.

The circular trajectory is used to validate the ellipsoidal set-membership estimation technique, whereas the aim of the linear trajectory is to estimate the components of the state vector and test them in a radar imaging application. More precisely, the goal is to calculate the frequencies for which the radar can operate; thus the need to compute the distance between the drone (i.e. the radar) and the target at each sample time. The guaranteed bounds for the relative distance provided by the set-membership state estimation technique are used to find the error on the estimation and the working frequency afterwards. The drone is initially, on the floor in an equilibrium state. The rotor's generated thrust compensates the weight. The estimation results have been obtained with an Intel Core i7 processor-3770 3.40 GHz. The entire flight duration for both trajectories is 235s. Both trajectories correspond first to a take-off to an altitude of 50m. The results for the take-off of the drone are the same for both movements regardless of the trajectory type. Figure 6 presents the guaranteed estimation bounds (blue dashed lines) of the altitude z , calculated using the technique previously detailed in Section 3. It can be seen that the real state (the red dots represented at each time instant in Fig. 6) is guaranteed to remain inside the estimated bounds (see the zoom of Fig. 6), despite the presence of perturbations and measurement noises. The velocity on the z-axis is shown in Fig. 7.

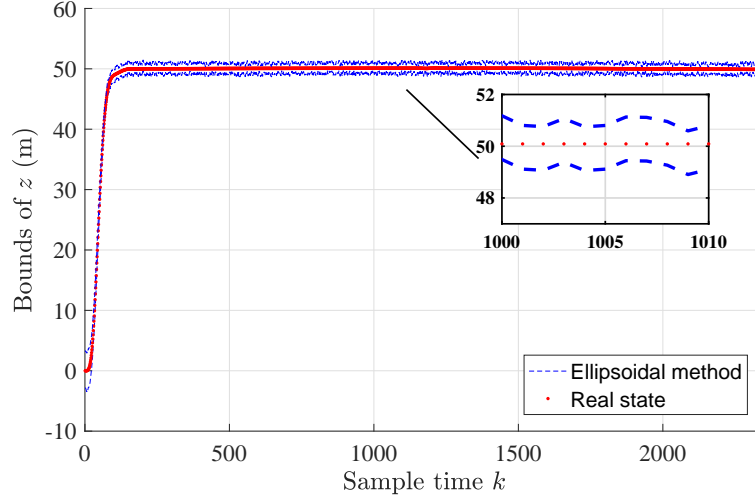


Figure 6. Estimation bounds of the altitude z

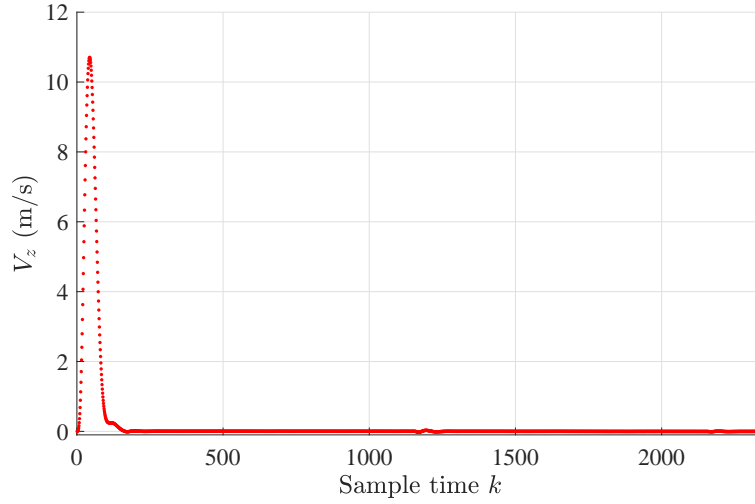


Figure 7. Drone's velocity on z-axis

In the next sections, the set-membership state estimation technique is validated through two different trajectories: a circular trajectory, and a linear trajectory suitable for the radar application.

5.1. Case 1: Circular Trajectory

After the take-off, the drone moves in a circular trajectory as shown in Fig. 8.

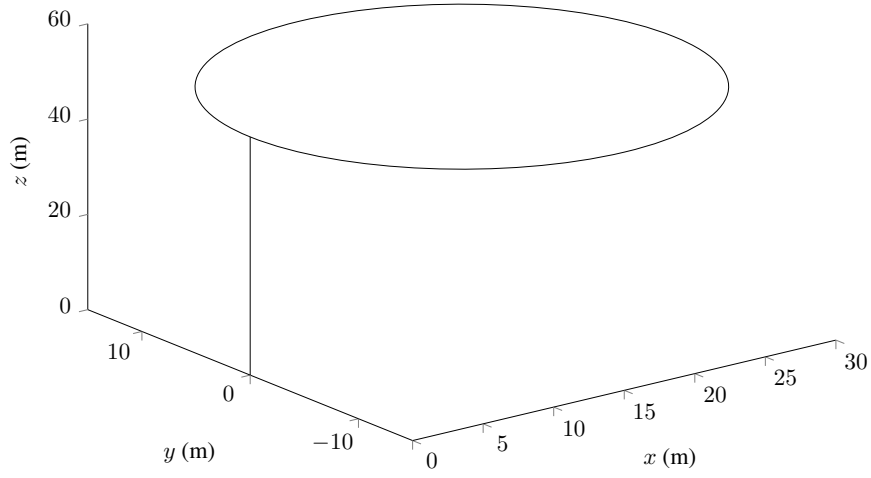


Figure 8. Circular reference trajectory

Figures 9 and 11 show the bounds of x and y , respectively computed as detailed in (7) applying the ellipsoidal set-membership state estimation method for 2350 iterations. The real state is represented by red dots and it is found inside the estimated bounds. Notice that at $t = 0$, the position of the drone is $(x_0, y_0) = (0, 0)$ and the velocity on both axes is equal to 0. The velocity of the drone varies between -2m/s and 2m/s as shown in Fig. 10 and Fig. 12.

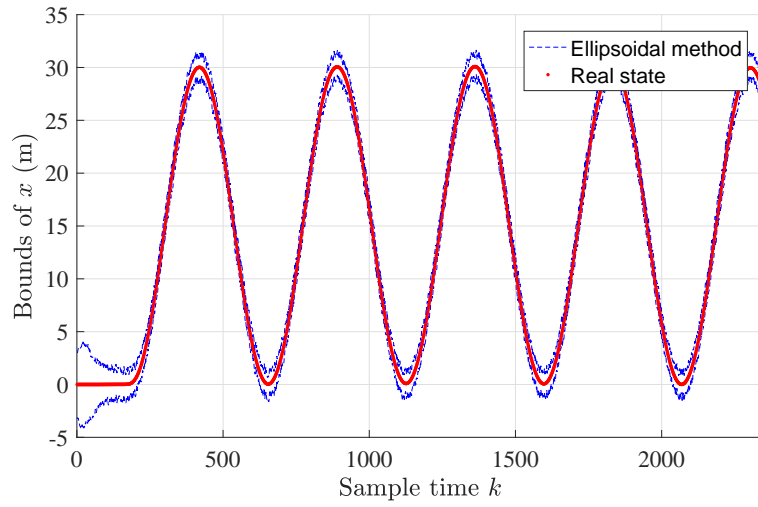


Figure 9. Estimation bounds of x

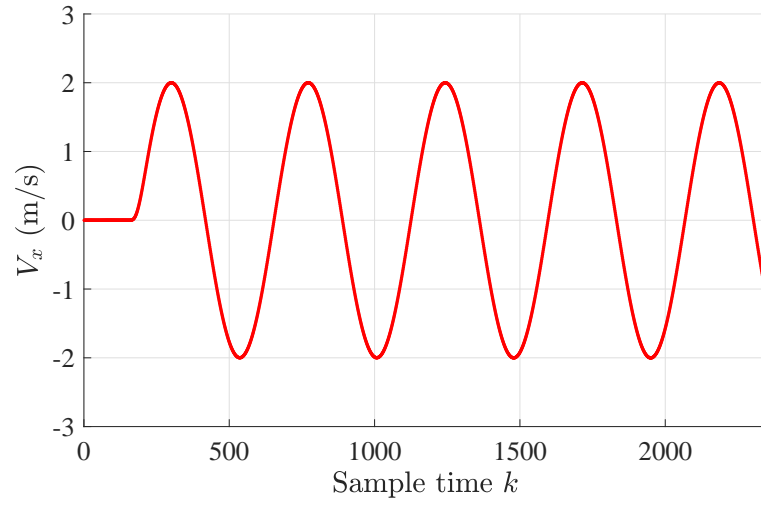


Figure 10. Drone's velocity on x-axis

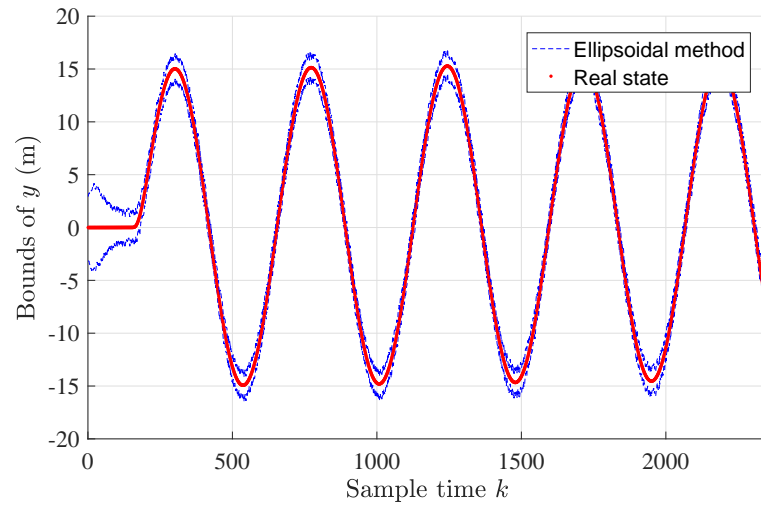


Figure 11. Estimation bounds of y

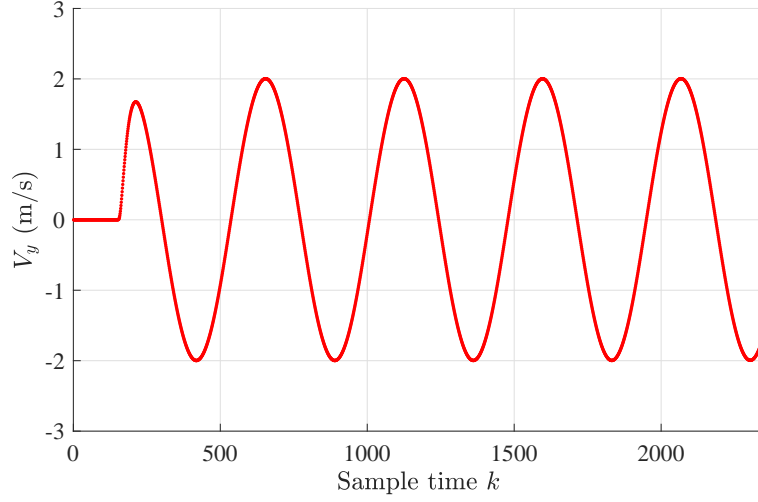


Figure 12. Drone's velocity on y-axis

5.2. Case 2: Linear Trajectory applied to SAR

After the take-off, the reference trajectory shown is composed of a movement on the x-axis from $x = 0$ to $x = 250\text{m}$ and then back to $x = 0$ at a constant speed of 2.5m/s , which is a relevant trajectory for the drone in a radar application. While the drone is moving, the radar scans a region where the potential target is expected. In details, the drone takes off from the initial starting point to reach a certain altitude. Then, it goes in an outward movement along the x-axis where it can scan a certain region before returning to its stopping point. These movements are represented in Fig. 13.

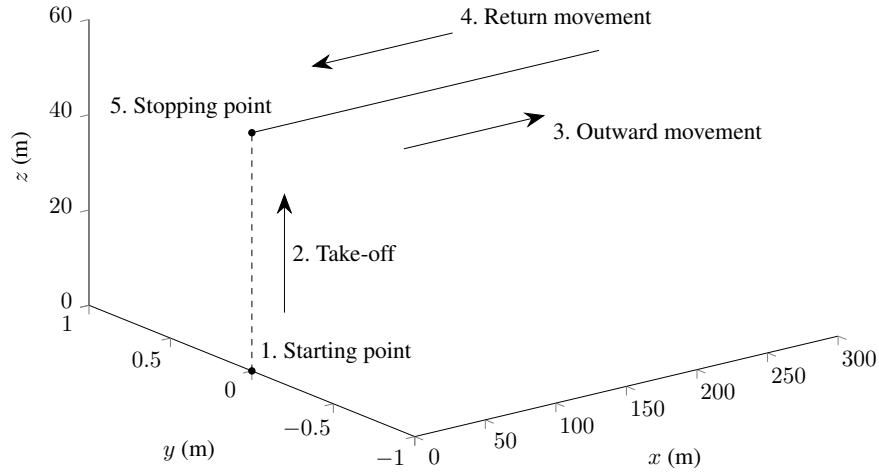


Figure 13. linear proposed trajectory

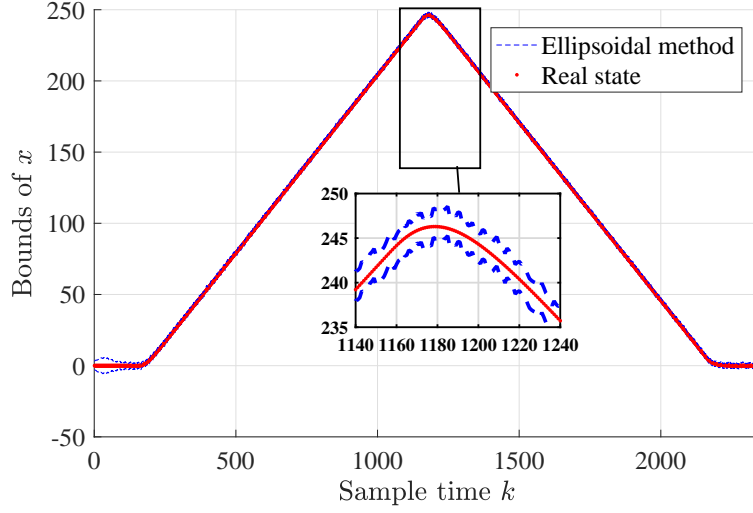


Figure 14. Estimation bounds of x

Figure 14 shows the estimation done on the drone's movement, along the x-axis. A part of the figure has been zoomed in order to better exhibit the position on the x-axis which is guaranteed inside the estimation bounds. The UAV keeps moving forward with a constant speed until it reaches its destination ($x = 250\text{m}$), this is when it moves in the opposite direction to reach the stopping point (Fig. 13) with the same speed as Fig. 15 shows. By the end, the drone would have scanned the area, and identified the targets, this is why the final velocity is equal to zero. It should be noticed that no movement is made on the y-axis, however (as shown in Fig. 16), the real y position is found between the upper and lower bounds (blue dashed curve in Fig. 16) estimated by the ellipsoidal technique.

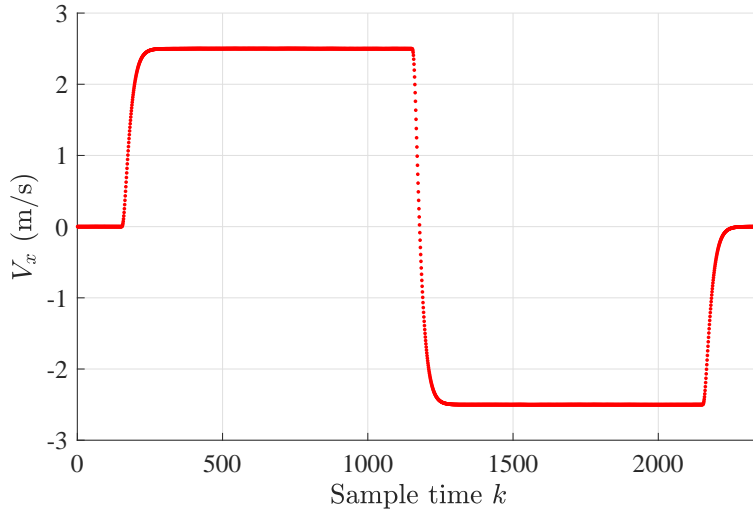


Figure 15. Drone's velocity on x-axis

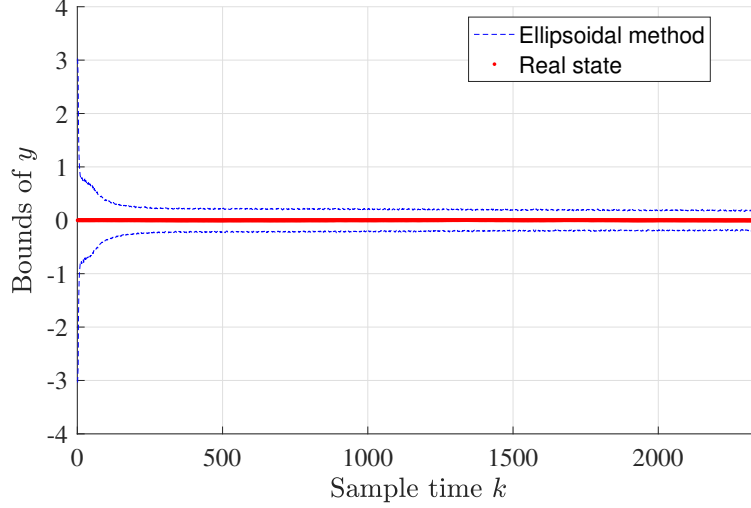


Figure 16. Estimation bounds of y

While moving in its planned linear trajectory, the drone images a scatterer during 8s (which corresponds to 20m for a nominal speed of 2.5m/s) in stripmap mode. An extreme case is considered here where the scatterer is at 50m range and 10m azimuth with respect to the scanned region (see Table 3).

Table 3. SAR parameters

PRF	2kHz
Scatterer position	
Azimuth	10m
Ground range	50m

Using the bounds found for the coordinates of the drone, the maximal, real and minimal distances between the scatterer and UAV are calculated at each iteration. Afterwards, $|D_{min} - D_r|$ and $|D_{max} - D_r|$ are plotted in Fig. 17, where δ_D is equal to $\max(\delta_{max}, \delta_{min})$. Since phase errors can be effectively compensated by autofocus techniques up to 60rad, and using (12) in Section 4 with $\delta_D \approx 2\text{m}$, the maximum operating frequency of the SAR sensor has to be less than 600MHz (very high frequency VHF and ultra high frequency UHF applications).

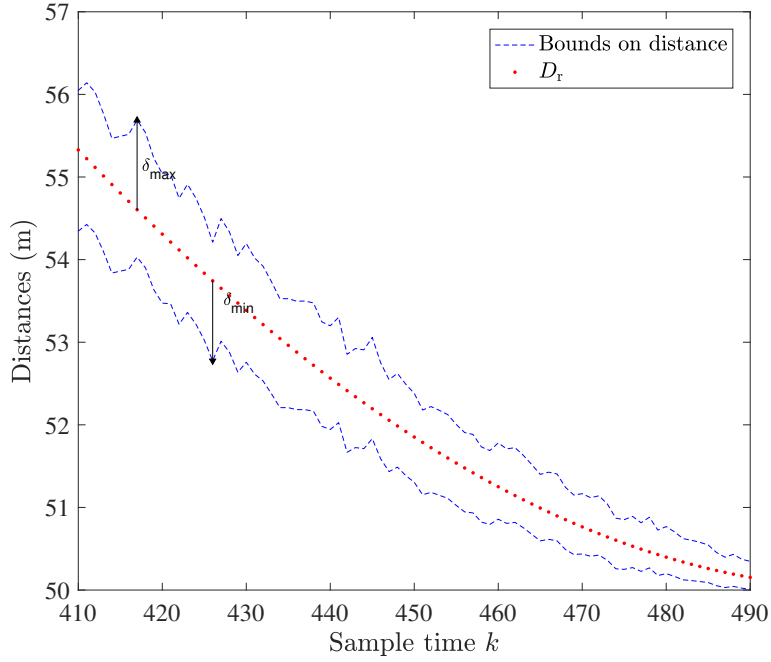


Figure 17. Distance errors

6. Conclusion

This paper illustrated an application of an ellipsoidal guaranteed set-membership state estimation technique to an octorotor's attitude and position used for radar applications. The considered technique minimizes an ellipsoidal set in the presence of bounded perturbations and measurement noises in order to improve the estimation accuracy at each sample time. The computed bounds are used in the context of radar applications to find the operating frequency of the synthetic aperture radar.

Future work consists on combining deterministic and stochastic approaches in a new state estimation technique that would improve performance. Other interesting perspectives are to consider model uncertainties, to extend the state estimation procedure for fault detection (e.g. actuator/sensor faults) or to extend the guaranteed ellipsoidal state estimation method for non-linear models. Finally, experimental tests will be considered to validate the methods on the UAV.

Acknowledgement

The authors acknowledge MEyC Spain (PID2019-106212RB-C41), the European Research Council and the UE ERDF (Advanced Grant OCONTSOLAR, Project ID: 789051).

References

- Abdolhosseini, M., Zhang, Y., & Rabbath, C. A. (2013). An efficient model predictive control scheme for an unmanned quadrotor helicopter. *Journal of Intelligent & Robotic Systems*, 70(1-4), 27–38.
- Alamo, T., Bravo, J. M., & Camacho, E. F. (2005). Guaranteed state estimation by zonotopes. *Automatica*, 41, 1035–1043.
- Ben Chabane, S., Stoica Maniu, C., Alamo, T., Camacho, E. F., & Dumur, D. (2014). A new approach for guaranteed ellipsoidal state estimation. *19th World Congress IFAC, Cape Town, South Africa*, 6533 - 6538.
- Ben Chabane, S. (2015). *Fault detection techniques based on set-membership state estimation for uncertain systems* (Doctoral dissertation). Université Paris-Saclay.
- Ben Chabane, S., Stoica Maniu, C., Alamo, T., Camacho, E. F., & Dumur, D. (2014). Ellipsoidal state estimation for systems with interval uncertainties. *IEEE Conference on Decision and Control, Los Angeles, United States*, 2603–2608.
- Ben Chabane, S., Stoica Maniu, C., Camacho, E. F., Alamo, T., & Dumur, D. (2016). Fault detection using set-membership estimation based on multiple model systems. *European Control Conference, Aalborg, Denmark*, 1105–1110.
- Bergman, K., & Ekström, J. (2014). *Modeling, estimation and attitude control of an octorotor using PID and L_1 adaptive control techniques* (Master’s thesis). Linkopings University - Sweden.
- Bertsekas, D., & Rhodes, I. (1971). Recursive state estimation for a set-membership description of uncertainty. *IEEE Transactions on Automatic Control*, 16(2), 117–128.
- Bhotto, M. Z. A., & Antoniou, A. (2011). Robust set-membership affine-projection adaptive-filtering algorithm. *IEEE Transactions on Signal Processing*, 60(1), 73–81.
- Carrara, W., Goodman, R., & Majewski, R. (1995). *Spotlight synthetic aperture radar: signal processing algorithms*. Artech House Inc.
- Casbeer, D. W., Beard, R. W., McLain, T. W., Li, S.-M., & Mehra, R. K. (2005). Forest fire monitoring with multiple small UAVs. *American Control Conference*, 3530–3535.
- Chachuat, B., Houska, B., Paulen, R., Peri’c, N., Rajyaguru, J., & Villanueva, M. E. (2015). Set-theoretic approaches in analysis, estimation and control of nonlinear systems. *9th IFAC Symposium on Advanced Control of Chemical Processes*, 48(8), 981 - 995.
- Chernousko, F. L. (1994). *State estimation for dynamic systems*. Boca Raton: CRC Press.
- Chevet, T., Makarov, M., Stoica Maniu, C., Hinostroza, I., & Tarascon, P. (2017). State estimation of an octorotor with unknown inputs. Application to radar imaging. *21st International Conference on System Theory, Control and Computing, Sinaia, Romania*, 723–728.
- Combastel, C. (2003). A state bounding observer based on zonotopes. In *European Control Conference* (p. 2589–2594). Cambridge, UK.
- Combastel, C. (2015). Zonotopes and Kalman observers: gain optimality under distinct uncertainty paradigms and robust convergence. *Automatica*, 55, 265–273.
- Daryin, A. N., & Kurzhanski, A. B. (2012). Estimation of reachability sets for large-scale uncertain systems: from theory to computation. *Proc. of IEEE Conference on Decision and Control, Maui, Hawaii, USA*, 7401–7406.
- Daryin, A. N., Kurzhanski, A. B., & Vostrikov, I. V. (2006). Reachability approaches and ellipsoidal techniques for closed-loop control of oscillating systems under uncertainty. *IEEE Conference on Decision and Control, San Diego, CA, USA*, 6390–6395.
- De Marina, H. G., Pereda, F. J., Giron-Sierra, J. M., & Espinosa, F. (2012). UAV attitude estimation using unscented Kalman filter and TRIAD. *IEEE Transactions on Industrial Electronics*, 59(11), 4465–4474.
- Durieu, C., Walter, E., & Polyak, B. (2001). Multi-Input Multi-Output ellipsoidal state bounding. *Journal of Optimization Theory and Applications*, 111(2), 273–303.
- Fogel, E., & Huang, Y. F. (1982). On the value of information in system identification-bounded noise case. *Automatica*, 18, 229–238.
- Garcia, R. A., Raffo, G. V., Ortega, M. G., & Rubio, F. R. (2015). Guaranteed quadrotor

- position estimation based on GPS refreshing measurements. *IFAC Workshop on Advanced Control and Navigation for Autonomous Aerospace Vehicles*, 48(9), 67-72.
- Gonzalez-Partida, J.-T., Almorox-Gonzalez, P., Burgos-Garcia, M., & Dorta-Naranjo, B.-P. (2008). SAR system for UAV operation with motion error compensation beyond the resolution cell. *Sensors*, vol. 8, no. 5, 3384-3405.
- Hausamann, D., Zirnig, W., Schreier, G., & Strobl, P. (2005). Monitoring of gas pipelines – A civil UAV application. *Aircraft Engineering and Aerospace Technology*, 77(5), 352–360.
- Hoffmann, H. H., Gabriel M., & Waslander, S. L. (2007). Quadrotor helicopter flight dynamics and control: Theory and experiment. *Proc. of the AIAA Guidance, Navigation, and Control Conference*.
- Kada, B., Munawar, K., Shaikh, M., Hussaini, M., & Al-Saggaf, U. (2016). UAV attitude estimation using nonlinear filtering and low-cost mems sensors. *7th IFAC Symposium on Mechatronic Systems*, 49, 521-528.
- Kalman, R. E. (1960). A new approach to linear filtering and prediction problems. *Transactions of the ASME–Journal of Basic Engineering*, 82(Series D), 35-45.
- Kingston, D., & Beard, R. (2004). Real-time attitude and position estimation for small UAVs using low-cost sensors. *AIAA 3rd Unmanned Unlimited Technical Conference, Workshop and Exhibit*, 6488.
- Kurzhanski, A. B., & Vályi, I. (1996). *Ellipsoidal calculus for estimation and control*. Birkhäuser Boston.
- Laliberte, A. S., & Rango, A. (2009). Texture and scale in object-based analysis of subdecimeter resolution unmanned aerial vehicle (UAV) imagery. *IEEE Transactions on Geoscience and Remote Sensing*, 47(3), 761-770.
- Le, V. T. H., Stoica, C., Alamo, T., Camacho, E. F., & Dumur, D. (2013). Zonotopic guaranteed state estimation for uncertain systems. *Automatica*, 49(1), 3418-3424.
- Lima, M. V., & Diniz, P. S. (2010). Steady-state analysis of the set-membership affine projection algorithm. In *2010 IEEE International Conference on Acoustics, Speech and Signal Processing* (pp. 3802–3805).
- Makarov, M., Stoica Maniu, C., Tebbani, S., Hinostroza, I., Moreira Beltrami, M., Kienitz, J., ... Rojas Lombarte, J. (2015). Octorotor UAVs for radar applications: modeling and analysis for control design. *Workshop on Research, Education and Development of Unmanned Aerial Systems, Cancun, Mexico*, 288-297.
- Merhy, D., Alamo, T., Stoica Maniu, C., & Camacho, E. F. (2018). Zonotopic constrained Kalman filter based on a dual formulation. In *IEEE Conference on Decision and Control, Orlando, Florida, United States* (pp. 6396–6401).
- Merhy, D., Stoica Maniu, C., Alamo, T., Camacho, E. F., & Ben Chabane, S. (2017). Comparison between two state estimation techniques for linear systems. *20th IFAC World Congress, Toulouse, France*, 4855-4859.
- Moreira, A., Prats-Iraola, P., Younis, M., Krieger, G., Hajnesk, I., & Papathanassiou, K. P. (2013). A tutorial on synthetic aperture radar. *IEEE Geoscience and Remote Sensing Magazine*, 6-43.
- Nesterov, Y., & Nemirovski, A. (1994). Interior point polynomial methods in convex programming: Theory and applications. *Society for Industrial and Applied Mathematics*.
- Nex, F., & Remondino, F. (2014). UAV for 3D mapping applications: A review. *Applied Geomatics*, 6(1), 1-15.
- Paulen, R., Villanueva, M. E., & Chachuat, B. (2016, Sep.). Guaranteed parameter estimation of non-linear dynamic systems using high-order bounding techniques with domain and cpu-time reduction strategies. *IMA Journal of Mathematical Control and Information*, 33(3), 563-587.
- Polyak, B., Nazin, S. A., Durieu, C., & Walter, E. (2004). Ellipsoidal parameter or state estimation under model uncertainty. *Automatica*, 40, 1171-1179.
- Pourasghar, M., Puig, V., & Ocampo-Martinez, C. (2016). Comparison of set-membership and interval observer approaches for state estimation of uncertain systems. *European Control Conference, Aalborg, Denmark*, 1111–1116.

- Puig, V. (2010). Fault diagnosis and fault tolerant control using set-membership approaches: Application to real case studies. *International Journal of Applied Mathematics and Computer Science*, 20(4), 619-635.
- Schweppe, F. C. (1968). Recursive state estimation: Unknown but bounded errors and system inputs. *IEEE Transactions on Automatic Control*, 13(1), 22-28.
- Streif, S., Kim, K.-K. K., Rumschinski, P., Kishida, M., Shen, D. E., Findeisen, R., & Braatz, R. D. (2013). Robustness analysis, prediction and estimation for uncertain biochemical networks. *10th IFAC International Symposium on Dynamics and Control of Process Systems, Mumbai, India*, 46(32), 1 - 20.
- Teixeira, B. O., Tórres, L. A., Iscold, P., & Aguirre, L. A. (2011). Flight path reconstruction—A comparison of nonlinear Kalman filter and smoother algorithms. *Aerospace Science and Technology*, 15(1), 60–71.
- Vandenberghe, L., & Boyd, S. (1994). Positive definite programming. *Mathematical Programming: State of the Art*, 276–308.
- Walter, E., & Piet-Lahanier, H. (1989). Exact recursive polyhedral description of the feasible parameter set for bounded-error models. *IEEE Transactions on Automatic Control*, 34(8), 911-915.
- Wang, Y., & Puig, V. (2016). Zonotopic extended Kalman filter and fault detection of discrete-time nonlinear systems applied to a quadrotor helicopter. *3rd Conference on Control and Fault-Tolerant Systems, Barcelona, Spain*, 367–372.
- Wang, Y., Puig, V., Cembrano, G., & Alamo, T. (2016). Guaranteed state estimation and fault detection based on zonotopes for differential-algebraic-equation systems. *3rd Conference on Control and Fault-Tolerant Systems*, 478-484.
- Werner, S., Apolinário Jr, J. A., & Diniz, P. S. (2007). Set-membership proportionate affine projection algorithms. *EURASIP Journal on Audio, Speech, and Music Processing*(1), 10–10.
- Werner, S., & Diniz, P. S. (2001). Set-membership affine projection algorithm. *IEEE Signal Processing Letters*, 8(8), 231–235.
- Yan, J., Guo, J., Wang, Q. L. K., & Liu, X. (2008). X-band mini SAR radar on eight-rotor mini-UAV. *IEEE Geoscience and Remote Sensing Symposium*, 6702-6705.
- Zaugg, E., Hudson, D., & Long, D. (2006). The BYU SAR: A small, student-built SAR for UAV operation. *IEEE Geoscience and Remote Sensing Symposium, Denver, Colorado, USA*, 411-414.